A&A 457, 79–90 (2006)
DOI: 10.1051/0004-6361:20065376

Astronomy & Astrophysics

The VIMOS VLT Deep Survey: the faint type-1 AGN sample⋆,⋆⋆

I. Gavignaud[1,2], A. Bongiorno[3], S. Paltani[4,5], G. Mathez[2], G. Zamorani[6], P. Møller[7], J. P. Picat[2], V. Le Brun[8], B. Marano[3], O. Le Fèvre[8], D. Bottini[9], B. Garilli[9], D. Maccagni[9], R. Scaramella[10,11], M. Scodeggio[9], L. Tresse[8], G. Vettolani[10], A. Zanichelli[10], C. Adami[8], M. Arnaboldi[12], S. Arnouts[8], S. Bardelli[6], M. Bolzonella[6], A. Cappi[6], S. Charlot[13,14], P. Ciliegi[6], T. Contini[2], S. Foucaud[9], P. Franzetti[9], L. Guzzo[15], O. Ilbert[3], A. Iovino[15], H. J. McCracken[14,16], C. Marinoni[18], A. Mazure[8], B. Meneux[9,15], R. Merighi[6], R. Pellò[2], A. Pollo[8], L. Pozzetti[6], M. Radovich[12], E. Zucca[6], M. Bondi[10], G. Busarello[12], O. Cucciati[15,17], S. de la Torre[8], L. Gregorini[10], F. Lamareille[2], Y. Mellier[14,16], P. Merluzzi[12], V. Ripepi[12], D. Rizzo[2], and D. Vergani[9]

[1] Astrophysikalisches Institut Potsdam, An der Sternwarte 16, 14482 Potsdam, Germany
e-mail: igavignaud@aip.de
[2] Laboratoire d'Astrophysique de l'Observatoire Midi-Pyrénées (UMR 5572), 14 avenue E. Belin, 31400 Toulouse, France
[3] Università di Bologna, Dipartimento di Astronomia, via Ranzani 1, 40127 Bologna, Italy
[4] Integral Science Data Centre, Ch. d'Écogia 16, 1290 Versoix
[5] Geneva Observatory, Ch. des Maillettes 51, 1290 Sauverny
[6] INAF – Osservatorio Astronomico di Bologna, via Ranzani 1, 40127 Bologna, Italy
[7] European Southern Observatory, Karl-Schwarzschild-Strasse 2, 85748 Garching bei München, Germany
[8] Laboratoire d'Astrophysique de Marseille – UMR 6110 CNRS, Université de Provence, BP 8, 13376 Marseille Cedex 12, France
[9] IASF – INAF, via Bassini 15, 20133 Milano, Italy
[10] IRA – INAF, via Gobetti 101, 40129 Bologna, Italy
[11] INAF – Osservatorio Astronomico di Roma, via di Frascati 33, 00040 Monte Porzio Catone, Italy
[12] INAF – Osservatorio Astronomico di Capodimonte, via Moiariello 16, 80131 Napoli, Italy
[13] Max Planck Institut fur Astrophysik, 85741 Garching, Germany
[14] Institut d'Astrophysique de Paris, UMR 7095, 98 bis Bvd Arago, 75014 Paris, France
[15] INAF – Osservatorio Astronomico di Brera, via Brera 28, Milan, Italy
[16] Observatoire de Paris, LERMA, 61 Avenue de l'Observatoire, 75014 Paris, France
[17] Universitá di Milano-Bicocca, Dipartimento di Fisica, Piazza delle Scienze 3, 20126 Milano, Italy
[18] Centre de Physique Théorique, UMR 6207 CNRS-Université de Provence, 13288 Marseille, France

Received 6 April 2006 / Accepted 24 May 2006

ABSTRACT

We present the type-1 active galactic nuclei (AGN) sample extracted from the VIMOS VLT Deep Survey's first observations of 21 000 spectra in 1.75 deg^2. This sample, which is purely magnitude-limited and free of morphological or color-selection biases, contains 130 broad-line AGN (BLAGN) spectra with redshift up to 5. Our data are divided into a wide ($I_{AB} \leq 22.5$) and a deep ($I_{AB} \leq 24$) subsample containing 56 and 74 objects, respectively. Because of its depth and selection criteria, this sample is uniquely suited for studying the population of faint type-1 AGN. Our measured surface density (~472 ± 48 BLAGN per square degree with $I_{AB} \leq 24$) is significantly higher than that of any other optically selected sample of BLAGN with spectroscopic confirmation. By applying a morphological and color analysis to our AGN sample, we find that (1) ~23% of the AGN brighter than $I_{AB} = 22.5$ are classified as extended, and this percentage increases to ~42% for those with $z < 1.6$; (2) a non-negligible fraction of our BLAGN are lying close to the color-space area occupied by stars in the $u^* - g'$ versus $g' - r'$ color-color diagram. This leads us to the conclusion that the classical optical-ultraviolet preselection technique, if employed at such deep magnitudes ($I_{AB} = 22.5$) in conjuction with a preselection of point-like sources, can miss up to ~35% of the AGN population. Finally, we present a composite spectrum of our sample of objects. While the continuum shape is very similar to that of the SDSS composite at short wavelengths, it is much redder than that of the SDSS composite at $\lambda \geq 3000$ Å. We interpret this as due to significant contamination from emission of the host galaxies, as expected from the faint absolute magnitudes sampled by our survey.

Key words. catalogs – surveys – galaxies: active – galaxies: Seyfert – quasars: general

1. Introduction

Recent surveys such as 2QZ and SDSS produce quasi-stellar object (QSO) spectra by the thousands (Croom et al. 2004; Richards et al. 2002), demonstrating the high efficiency of optical color-selection techniques used since the pioneering work by Sandage & Wyndham (1965). Spectroscopic targets are preselected based on their location in multidimensional color space

⋆ Based on data obtained with the European Southern Observatory Very Large Telescope, Paranal, Chile, program 070.A-9007(A), 272.A-5047, 076.A-0808, and on data obtained at the Canada-France-Hawaii Telescope, operated by the CNRS of France, CNRC in Canada, and the University of Hawaii.

⋆⋆ Appendix is only available in electronic form at http://www.edpsciences.org

(far from main sequence stars) and their morphology (point-like appearance to avoid galaxies). The drawback of such prerequisites is that some subsets of the underlying QSO population may be under-represented in these surveys, thereby possibly biasing our current understanding of this population of objects.

The preselection of non-resolved objects prevents the selection of faint active nuclei in relatively bright galaxies and introduces incompleteness at low redshift. Moreover, the selection of unresolved objects is highly dependent on the quality of the imaging data. The ultraviolet (UV) excess selection is efficient only up to $z \sim 2.3$, and the evolving track of standard QSO crosses over main sequence stars near $z \sim 2.5 \pm 0.5$ in most optical broad-band color-color planes. While it is difficult to identify AGN candidates in this redshift range, it is also at this epoch that a maximum in the QSO space density seems to be observed (Wall et al. 2005), although there is now a clear indication, at least for the X-ray selected AGN, that this maximum is dependent on the intrinsic luminosity (Hasinger et al. 2005). It is therefore essential to obtain unbiased samples at these high redshifts to trace and understand the history of accretion onto supermassive black holes, which is believed to be the origin of the AGN phenomena.

Other criteria have been used to select AGN samples, including spectral energy distribution of objects in slitless spectroscopic plates (Hewett et al. 1995; Wisotzki et al. 2000), variability and low proper motion (Brunzendorf & Meusinger 2002), or radio emission (Jackson et al. 2002; Ivezić et al. 2002), but they are always biased toward some subsets of the population. X-ray surveys are an efficient alternative to traditional, optically-selected samples and, indeed, they have allowed the luminosity function and the evolution of various classes of X-ray emitting AGN to be derived, with good statistics (e.g. absorbed and unabsorbed AGN in the X-ray band, soft and hard X-ray selected, see Miyaji et al. 2000; Ueda et al. 2003; Hasinger et al. 2005). However, comparing the results obtained for X-ray and optically selected AGN is not straightforward both because of the different composition of the samples (X-ray samples contain a large fraction of obscured AGN, without broad emission lines in their optical spectra) and of the somewhat different definition of AGN that is usually adopted in the X-ray surveys (e.g. any source with an X-ray luminosity and/or an X-ray to optical luminosity ratio above given thresholds).

Identifying faint type I AGN in a complete magnitude-limited optical sample has been attempted in the Canada France Redshift Survey (CFRS) with 6 QSO identified among 943 spectra down to a limiting magnitude of $I_{\rm AB} = 22.5$ (Schade et al. 1996).

To probe fainter magnitude, the COMBO-17 project identifies AGN from their spectral energy distribution (SED) based on photometry in a set of 17 filters. They selected 192 objects over 0.78 square degrees down to a magnitude $R = 24$ with $z > 1.2$ (Wolf et al. 2003). Although the technique developed by this team leads to a good redshift accuracy ($\Delta z \sim 0.03$), it can be affected by some "catastrophic errors" in the region of the color space where various identifications are possible or in the case of objects with SED deviating from the reference set of templates.

In this paper we present a spectroscopic catalog of broad emission-line objects obtained from the purely flux-limited spectroscopic sample of the VIMOS VLT Deep Survey (VVDS). This sample, free of any color or morphological biases, can be considered as a minimally biased sample for exploring the population of optically non-obscured QSO at the faint end of the luminosity function. Our completeness is essentially set by the *S/N* ratio at which a broad emission line can be reliably identified in our spectra.

The data are divided into a wide ($I_{\rm AB} \leq 22.5$) and a deep ($I_{\rm AB} \leq 24$) subsample containing 56 and 74 objects, respectively. The limiting magnitude of our deep sample is well beyond the limit of the other optical spectroscopic surveys of AGN.

In the following section we briefly describe the VVDS imaging and spectroscopic surveys. In Sects. 3 and 4 we describe the process of AGN identification in the VVDS and the corresponding selection function. In Sects. 5, 6, and 7 we present the surface density of BLAGN, the redshift distribution, and the morphological and color properties of our sample. The composite spectrum of our sample of objects is presented and discussed in Sect. 8.

2. Observations

The VVDS[1] is a faint-imaging and $I_{\rm AB}$ magnitude-limited spectroscopic survey. The spectroscopic VVDS survey consists of the VVDS-deep, targeting objects in the range $I_{\rm AB} = 17.5{-}24.0$, and the VVDS-wide, targeting objects in the range $I_{\rm AB} = 17.5{-}22.5$.

The purely magnitude-limited selection of spectroscopic targets was carried out from a catalog based on deep photometry. This catalog is complete down to $I_{\rm AB} = 25$ in all fields. In addition, deep multi-band photometry was obtained, providing comprehensive multi-wavelength information for the objects. The B, V, R, and I photometry was obtained on the full fields of view and U, K, and J in smaller areas. For a detailed description of the photometric catalog we refer the reader to Le Fèvre et al. (2004). A comprehensive description of the data reduction and final data quality of the deep imaging survey can be found in McCracken et al. (2003).

Spectroscopic observations were performed with the multi-object spectrograph VIMOS installed on Melipal (see Le Fèvre et al. 2003), the third 8-meter telescope at Paranal Observatory. In this paper we present results based on the first spectroscopic runs only (Epoch One), obtained during October and November 2002. These observations and the reduction procedure are presented in detail in Le Fèvre et al. (2005) for the deep survey and in Garilli et al. (2006) for the wide sample.

2.1. The VVDS multi-wavelength imaging survey

The wide and deep fields were imaged in four bands, B, V, R, and I. The wide photometric survey covers 12 deg^2 in three high-galactic latitude fields, each 2×2 deg^2: VVDS-1003+01, VVDS-1400+05, and VVDS-2217+00. The deep photometric survey covers a 1.3×1 deg area, VVDS-0226-04. Part of the deep field as been observed in additional bands: U (Radovich et al. 2004), J and K (Iovino et al. 2005), u^*, g', r', i', z' from the Canada-France-Hawaii Legacy Survey (CFHTLS)[2], as well as in radio (1.4 GHz) on the VLA (Bondi et al. 2003), X-ray with XMM (Pierre et al. 2004), and UV with Galex (Arnouts et al. 2005; Schiminovich et al. 2005).

In order to avoid surface brightness selection biases down to the faintest required spectroscopic limit of $I_{\rm AB} = 24$, the imaging survey was designed to be complete down to $I_{\rm AB} = 25$ (see McCracken et al. 2003). The B, V, R, and I observations were performed from November 1999 to October 2000 at the 3.6 m Canada-France-Hawaii Telescope, with the CFH12K wide-field mosaic camera.

[1] http://www.oamp.fr/virmos/vvds.htm
[2] www.cfht.hawaii.edu/Science/CFHLS

Table 1. Summary of some of the spectroscopic data available on VVDS first-epoch fields.

Field	Mode	TSR*	$\mathcal{A}^{**}$ [deg^2]
VVDS-0226-04	deep	25%	0.48
VVDS-1003+01	wide	26%	0.33
VVDS-2217+00	wide	22%	0.81
CDFS	deep	23%	0.13

* Target sampling rate: fraction of objects in the photometric catalog inside our targeted area $\mathcal{A}$, which have been spectroscopically observed.
** Geometrical area in deg^2 of the spectroscopic first-epoch data that are used in this work.

In addition to the VVDS fields, a deep spectroscopic survey was also performed in 0.13 deg^2 of the Chandra Deep Field South (CDFS) field and is included in this work. This field is based on the EIS *I* band catalog described in Arnouts et al. (2001). The spectroscopic data available in the CDFS are public and are described in Le Fèvre et al. (2004).

All magnitudes given in this paper are corrected for galactic extinction using the dust map provided by Schlegel et al. (1998).

2.2. Target selection

To get a fully unbiased spectroscopic sample, one would pick objects at random from the input catalog. But such a procedure could then provide spectra at a less-than-optimal rate for a given observing time. For this reason a special target-selection algorithm SPOC was developed, with the aim of optimizing the use of spectroscopic follow-up time given the constraints of the VIMOS optical and mechanical layout (Bottini et al. 2005). In this optimization process, however, two biases are introduced.

First, objects with a small projected size along the slit are slightly favored for spectroscopic selection, resulting in a bias against more extended objects. This bias has to be taken into account in our analysis (as described in Sect. 4.1). Second, the distribution of selected targets is not isotropic as SPOC prevents the observation of targets closer than 2′ perpendicular to the slit direction to avoid surperpositions of spectra. However, this bias is only relevant for studies related to correlation function and large-scale structure (see Pollo et al. 2005), so it can be ignored here.

2.3. Spectroscopy

The area covered by the Epoch One VVDS spectroscopy is ∼0.6 deg^2 in the deep fields and ∼1.1 deg^2 in the wide fields (see Col. 4 in Table 1) and the corresponding numbers of spectra are 11 564 and 9440, respectively. The target sampling rate, i.e. the ratio of selected objects for spectroscopy to the total number of objects down to the respective spectroscopic flux limits, is ∼25% in both the wide and the deep surveys.

We used VIMOS' low-resolution red grism, which covers the wavelength range 5500−9500 Å with a 7 Å/pixel dispersion. The slit width was fixed to 1″, providing a sampling of 5 pixels per slit and a spectral resolution of $R \sim 230$ corresponding to a spectral-resolution element of ∼33 Å. The total integration time is 4.5 h per mask in the deep fields and 50 min in the wide fields. Data reduction was performed homogeneously using the VIPGI software, which was developed specifically for the VVDS survey Scodeggio et al. (2005).

The measured median *S/N* per resolution element at our limiting magnitudes is 4 in both the deep and wide fields. This is sufficient for detecting the main broad emission lines in a typical BLAGN spectrum.

3. Spectral classification

The process of classification and redshift determination of the reduced VVDS spectra is described in Le Fèvre et al. (2005). As an integrated part of this process, all objects with broad emission lines are identified and flagged. When only narrow emission lines are present, it is not straightforward to recognize AGN activity (type-2 AGN) from starburst activity, especially in spectra with relatively low *S/N* and limited wavelength range. For this reason we have chosen not to include narrow-line AGN in our present catalog. This population of objects will be presented in forthcoming publications.

We will now focus on the BLAGN catalog that consists of the sub-sample of objects in the VVDS spectroscopic catalog identified purely on the basis of the presence of one or more broad emission lines.

3.1. The BLAGN catalog

We have selected objects with broad lines that have a full-width half maximum (*FWHM*) larger than 1000 km s^{-1}, which offers a secure threshold compared to our spectral resolution. We make no distinction between Seyfert galaxies and QSOs based on the absolute magnitude or morphology of the objects.

The sample of BLAGN spectra selected from the VVDS survey consists of 56 objects from the wide fields ("the wide BLAGN sample") and 74 objects from the deep fields ("the deep BLAGN sample"). The total number of 130 BLAGN corresponds to about 0.7% of the objects in the total VVDS database with a measured redshift. Not all of the selected 130 BLAGN have a secure redshift. In some cases, we have two or more possible redshifts for a given object ("redshift degeneracy").

3.2. Redshift degeneracy

The exact list of emission lines we expect to detect in any given spectrum is a function of its *S/N*. In addition, because of the limited wavelength coverage of the observations, there are some redshift intervals where only a single broad emission line can be detected in our spectra (see Fig. 1). In these cases, if no other features (e.g. narrow emission lines, absorption systems, Lyman forest) are present, several interpretations of the broad line may be allowed, thereby leading to a degeneracy of solutions for the redshift (see an example in Fig. 3).

In order to treat redshift degeneracy in a consistent way, we took the SDSS composite spectrum of BLAGN (Vanden Berk et al. 2001), convolved it to our resolution, and added noise. For each line we then determined the *S/N* that would provide a 3.5σ detection of the line. Following this procedure we have found that down to a *S/N* of 4 per resolution element, we are able to detect and recognize the following lines as broad: Hα 6563, Hβ 4861, MgII 2799, C III] 1909, C IV 1549 and Lyα 1216.

The visibility windows of these lines within the VVDS-observed spectral range are shown in Fig. 1 as a function of redshift. The redshift ranges where we expect to observe a single broad emission line (in gray) are: [0−0.13], [1.0−1.9], and [2.4−2.6].

Since we always expect to detect the narrow-emission-line doublet [OIII] 4959 5007 close to Hβ, we consider that detection of Hβ securely identifies the redshift. The same applies to Lyα,

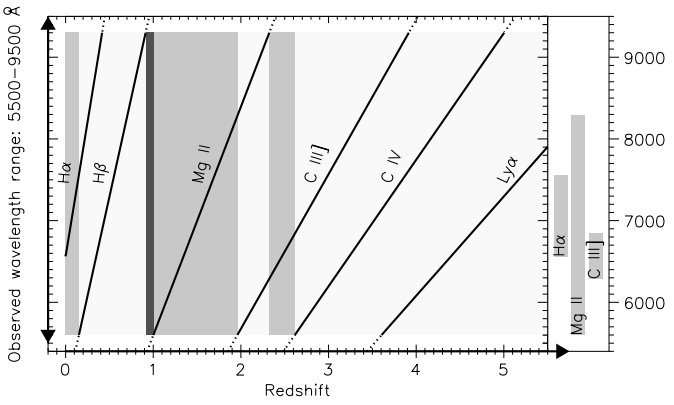

Fig. 1. Visibility in the wavelength range of our data of AGN broad emission lines along redshift: the thick lines trace the observed wavelength as a function of redshift of the main AGN broad emission lines that we expect to detect in our spectra. The objects in which we detect only a single broad emission line are expected to be in the redshift ranges shown in light gray. We expect to miss BLAGN lying in the narrow redshift range filled in dark gray since no strong broad emission line is visible at that redshift within our observed wavelength window. On the right side are reported the wavelength ranges in which each broad emission line can be observed as isolated. Hβ and Lyα are not reported there since they are not concerned by the redshift degeneracy.

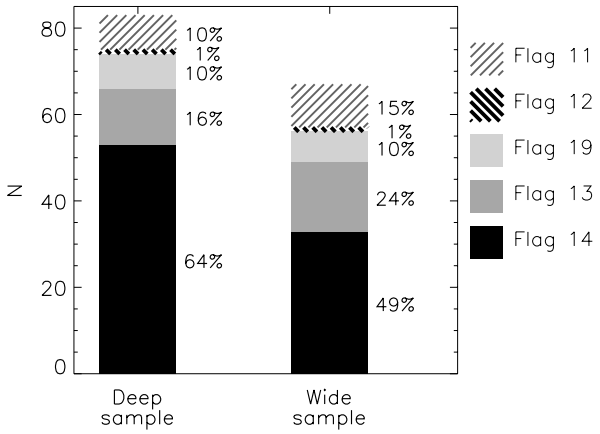

Fig. 2. AGN quality flags statistics.

which can be identified from the Lyman forest. Consequently, for an object with a single broad line, we have one to three potential redshifts. In addition, a small gap is present at redshift ∼0.95 (Fig. 1), where no broad emission line is visible within our observed wavelength window. A small fraction of spectra (∼15%) fall outside this general scheme, due to a lower *S/N* or to technical limitations such as strong fringing. For this reason some objects have up to four possible redshifts.

Because of these limitations, a total of 42 BLAGN in our original sample were flagged as having a degenerate redshift (Flag 19, as defined Sect. 3.3). To solve this redshift degeneracy, we first looked for the objects already observed in other spectroscopic surveys in the same areas. From the CDFS optical spectroscopic data we found the redshifts of 3 of the objects (Szokoly et al. 2004). Furthermore, additional observations were obtained with FORS1 on the VLT in March 2004 and November 2005 to extend the spectral coverage down to 3800 Å. From these observations we were able to solve the redshift degeneracy and find a secure redshift for 25 objects. The fraction of BLAGN remaining with a degenerate redshift corresponds to ∼10% of the total BLAGN sample.

3.3. Identification and redshift quality flags

Based on the above analysis, each entry of our BLAGN catalog has been assigned a quality flag according to the following criteria (these flags have been adapted from the VVDS galaxy flag definition):

Flag 14: BLAGN with secure redshift measurement (i.e.: two lines or more);

Flag 13: BLAGN with only one line detection but with the redshift secured from other informations such as:
- no other possible identification for the given wavelength range;
- an intervening absorption-line system is detected, which this leaves only one redshift solution for the BLAGN;
- strong iron features, so-called "bumps", are detected;
- a second line is marginally detected;

Flag 19: BLAGN with only one detected line and more than one possible redshift;

Flag 12: object with secure redshift but for which the broad-line nature is uncertain due to the low spectral resolution, often coupled with low *S/N* or with technical limitations (i.e. it could be a narrow-line object);

Flag 11: both the redshift and the broad-line nature of the target are uncertain.

The statistics of the data quality according to these flags is summarized in Fig. 2. Objects with uncertain broad emission lines (flags 11 and 12), corresponding to ∼(10−15)% of our survey objects, are excluded from the present analysis, since we do not want to be contaminated by normal galaxies and do not know which proportion of these objects are really broad-line AGN. The final sample of BLAGN with secure classification (flag 14, 13, and 19), used in the statistical analysis, contains 130 objects. They are presented in Appendix A: Table A.1 gives the list of BLAGN in the wide and deep samples for which we have a secure redshift, while Table A.2 lists the BLAGN for which we still have a redshift degeneracy (flag 19).

Figure 3 presents some examples of spectra across our magnitude and redshift range. In particular, object 220567224 is the highest redshift BLAGN discovered with this survey; object 020180665 is an example of a broad-absorption-line (BAL) spectrum, while object 020302785 is instead a BLAGN at $z = 2.24$ in which there are evident absorption features that can be well fitted by metal absorptions of a system at $z \sim 1.727$. Object 020463196 is an example of AGN in which strong [NeIII], [NeIV], and [NeV] lines are visible, and object 220098629 is an example of flag 19 for which the redshift was resolved with additional observations obtained with F0RS1.

4. Selection function

To study the statistical properties of the VVDS BLAGN sample we need to correct for the BLAGN that have not been spectroscopically observed and for the BLAGN that were not correctly identified from their spectrum. This correction is performed by applying two statistical weights to our BLAGN, $w^{\rm TSR}$ and $w^{\rm SSR}$ defined hereafter following Ilbert et al. (2005).

4.1. Treatment of non-targeted BLAGN: $w^{\rm TSR}$

The *target sampling rate* (hereafter TSR) is the fraction of objects in the photometric catalog inside our targeted area that

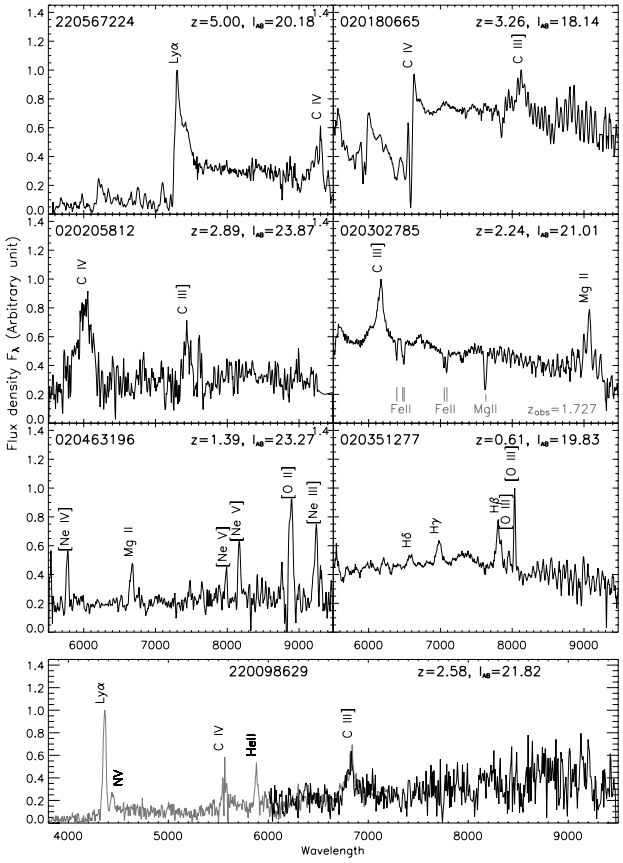

Fig. 3. Examples of BLAGN spectra across our magnitude and redshift ranges. Spectra of AGN with $I_{AB} > 23$ were rebinned to 5 pixels.

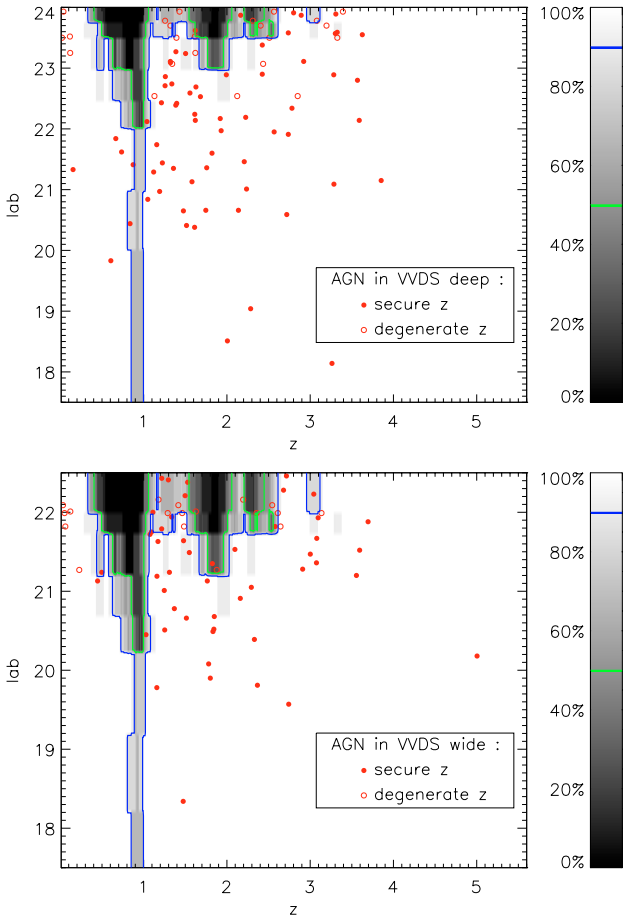

Fig. 4. *Spectroscopic success rate* for BLAGN in the VVDS deep (*top*) and wide (*bottom*) sample as a function of redshift and apparent magnitude. Contour lines are drawn for 90% and 50% of the identification success rate. The location of BLAGN with a secure redshift is reported with filled dots. BLAGN with a degenerate redshift are plotted at their different redshift solutions with open circles.

have been spectroscopically observed. As already mentioned in Sect. 2.2, the TSR is a function of the projected size, $x - radius$, of the objects along the slits. Objects with a small x-radius are slightly favored by the selection process. To balance for non-targeted BLAGN, we apply the weight $w^{TSR} = \frac{1}{TSR}$ to our BLAGN.

4.2. Treatment of misclassified AGN: w^{SSR}

The *spectroscopic success rate* (SSR) is the probability of a spectroscopically targeted object to be securely identified. It is a complex function of the BLAGN redshift, apparent magnitude, and intrinsic spectral energy distribution. To evaluate the SSR, we simulated 20 Vimos pointings for a total of 2745 spectra. The simulations incorporate the major instrumental effects of Vimos observations, including sensitivity curve, fringing in the redmost part of the spectra, sky background, and contamination by zeroth-orders. Each spectrum has been simulated using the SDSS composite spectrum as a template. Redshifts and magnitude were drawn at random in the ranges $0 < z \leq 5$ and $17.5 \leq I \leq 24$, respectively. The spectra were then analyzed and classified in the same way as the real spectra, except that we did not try to resolve cases where a single line was present; we merely checked whether the BLAGN nature of the object could be detected in the spectrum or not. Figure 4 presents the resulting SSR as a function of redshift and apparent I_{AB} magnitude in the deep and wide fields. To correct for missed BLAGN, we applied to our objects the weight $w^{SSR} = \frac{1}{SSR}$.

Objects for which the broad-line equivalent width (EW) is larger than in the SDSS composite spectrum will be over-estimated by our method and, in contrast, objects with weaker broad emission lines will be under-estimated. We investigated in particular the differences in the SSR that are expected for AGN with the emission-line properties of our composite spectrum (see Sect. 8 and Table 3). We found this difference to be small.

Correction for our global selection function is obtained by applying the product of these two weights, i.e. $w^{TSR} \times w^{SSR}$ to each of our objects.

Table 2. BLAGN number counts as a function of I_{AB} magnitude. N is the actual number of BLAGN in the VVDS survey, while $\mathcal{N}(\leq I_{AB})$ is the cumulative surface density of BLAGN (objects / square degree) corrected for incompleteness.

I_{AB}	N	$\mathcal{N}(\leq I_{AB})$
19	3	10
20	9	22
21	29	71
22	76	196
23	108	327
24	130	472

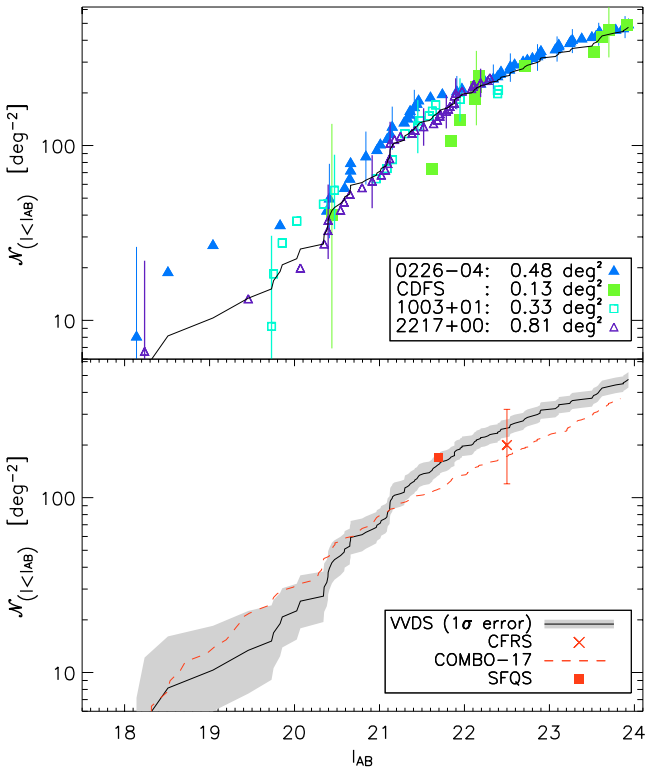

Fig. 5. BLAGN cumulative surface density in the VVDS sample. Error bars are the one-sigma Poissonian errors. *Top panel*: observed surface density in the individual fields and in the total sample (solid line). For readability, error bars are reported for each 5 data points. *Bottom panel*: comparison with CFRS and COMBO-17 surveys.

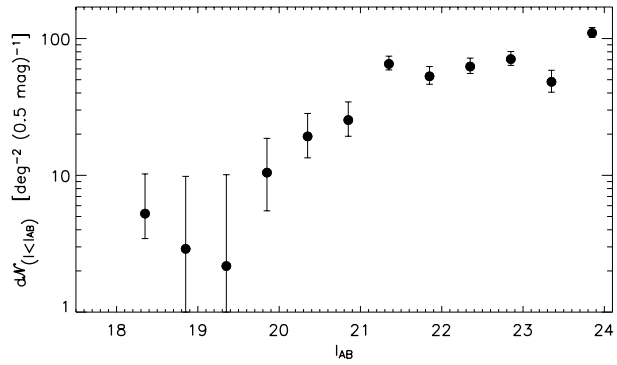

Fig. 6. BLAGN differential surface density in the VVDS sample. Error bars are the one-sigma Poissonian errors.

5. Counts

Since the objects to be observed spectroscopically in the VVDS are selected on the basis of their I_{AB} band magnitude, we computed the BLAGN cumulative surface density in this band with the following algorithm:

$$\mathcal{N}(\leq I_{AB}) = \frac{1}{\mathcal{A}} \sum_{i, I_{AB,i} \leq I_{AB}} w_i^{TSR} w_i^{SSR},$$

where $\mathcal{A}$ is the geometrical area targeted by the spectroscopic survey (i.e. the area covered by the different VIMOS fields of view corrected for the area masked in our photometric catalogs), and where the sum is running over all BLAGN i with magnitude I_i less or equal to I_{AB}.

The upper panel of Fig. 5 presents the cumulative surface density derived in the VVDS individual fields with the corresponding Poissonian error bars (Gehrels 1986). Although some differences in the counts in different fields are visible, the surface densities measured in all our fields at $I_{AB} = 22.5$, corresponding to the magnitude limit of the wide fields, are all consistent, within the errors. We conclude that the error induced by cosmic variance is smaller than our Poissonian noise. We compute a single $\log \mathcal{N} - I_{AB}$ curve by merging the data from the four fields into a single coherent sample (Avni & Bahcall 1980). At the limit of our deep fields ($I_{AB} < 24.0$) our measured surface density of BLAGN is ~472 ± 48 per square degree, and the correction applied for misclassified BLAGN corresponds to ~10% of this value. The differential surface density computed for the total sample is shown in Fig. 6. In this plot the different points and associated errors are independent of each other. This figure suggests a significant turnover in the slope of the counts at $I_{AB} \sim 21.5$. At $I_{AB} \gtrsim 21.5$ the differential number counts still increase with magnitude, but at a much lower rate than at brighter magnitudes. This effect is seen, although less clearly, in the continuous flattening with magnitude of the integral number counts in Fig. 5.

Comparison with other spectroscopic surveys is not straightforward since most of the optical QSO surveys are based on much shallower B-band flux-limited samples, and most of them are not complete over the entire redshift range due to their different selection criteria. The CFRS is an exception with essentially the same selection function as the VVDS (i.e. a flux-limited sample in the I band with no color or morphological selection). Although it contains only 6 BLAGN at a magnitude limit of $I_{AB} < 22.5$ (see Schade et al. 1996), the surface density resulting from these objects is in excellent agreement with our current measurement (see Fig. 5, lower panel).

The surface density derived from the recent SDSS Faint Quasar Survey (SFQS Jiang et al. 2006) is also reported in Fig. 5, lower panel. This survey selects AGN over $0 < z < 5$ up to $g = 22.5$. The surface density, corrected for completeness, is computed in the g band (Jiang, private communication) and approximately translated to the I_{AB} band assuming the mean color term observed in our sample: $\langle I_{AB} - g \rangle = -0.7$. The VVDS and SFQS number counts at $I_{AB} \sim 21.8$ are in good agreement.

With a limiting magnitude similar to ours the only other comparable sample is the COMBO-17 sample (see Wolf et al. 2003), which is based, however, on photometric selection of AGN, with a small fraction of spectroscopic confirmation. For comparison with our sample, we obtained the complete COMBO-17 sample cumulative counts, without redshift restriction (Wisotzki, private communication). Since this sample is selected in R-band, we apply a global color term of −0.16 mag to translate their surface density to our I_{AB} reference system. This color term corresponds to the mean $I_{AB} - R_{vega}$ color observed for our objects. In addition, a dozen BLAGN are observed in both VVDS and COMBO-17 samples. The mean color term of these objects is measured to be −0.12, and the result is presented in the lower panel of Fig. 5. Our number counts are statistically consistent with COMBO-17 for magnitudes brighter than 21.5. At fainter magnitude, our counts are systematically higher by ~30−40%. This can be explained by incompleteness in the COMBO-17 at low redshift in the regime where the host galaxy contamination becomes non-negligible. This is why the published version of the COMBO-17 AGN sample was restricted to $z > 1.2$. When restricting our sample to $z > 1.2$ and computing our surface density in the R band, we

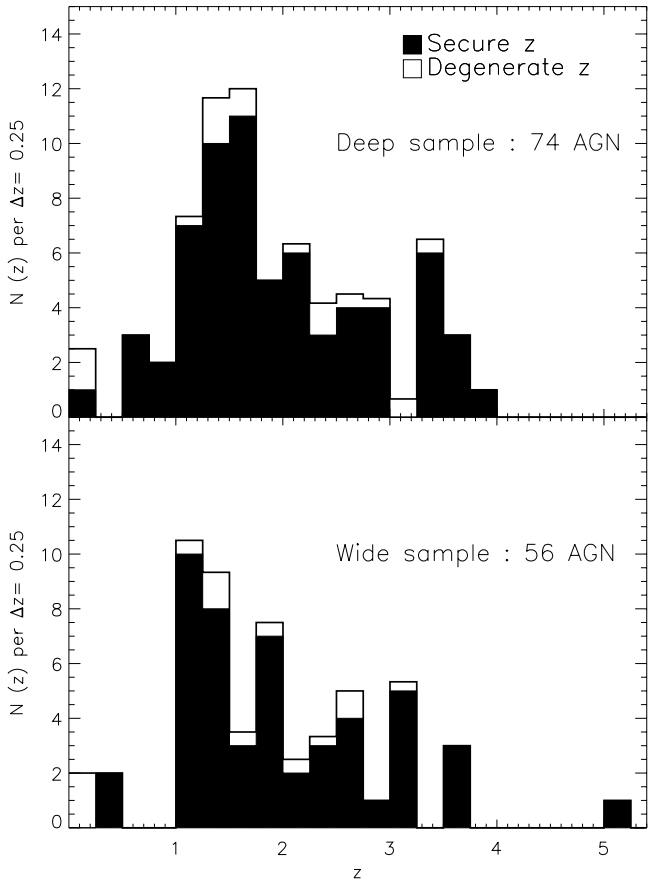

Fig. 7. Redshift distribution of the VVDS BLAGN sample. The shaded histogram corresponds to BLAGN with a secure redshift (flags 13 and 14), while the unshaded histogram also includes flag 19 BLAGN, distributed with an equal weight over the different redshift alternatives.

find $\mathcal{N}(R \leq 24) = 340 \pm 47$, which compares well with the published result of COMBO-17 sample $\mathcal{N}(R \leq 24) = 337$.

6. Redshift distribution

The redshift distributions of our wide and deep samples are presented in Fig. 7. BLAGN with degenerate redshift solution (flag 19) were distributed with equal weights in the different possible redshifts. The absence of objects between redshift 0.5 and 1 in the wide fields can be attributed to our low efficiency for selecting objects at this redshift (see Fig. 4). The main uncertainty resulting from BLAGN with a degenerate redshift concerns the fraction of BLAGN at low redshift.

The fraction of $z > 3$ objects is ∼17% in the wide sample and ∼15% in the deep sample. The mean redshift is ∼1.8 in both the wide and deep samples. When considering all flag 19 BLAGN successively at their lower and higher redshift solution, we find that the mean redshift of both deep and wide sample lies between 1.5 and 2.1. This shows that, by pushing our limit in magnitude from the wide to the deep surveys, we are not increasing our mean redshift but rather exploring the fainter part of the luminosity function at all redshifts.

Figure 8 shows the apparent magnitude versus redshift distribution of BLAGN and galaxies in the deep sample. We see that some of our BLAGN are sampling the faint magnitudes, well inside the galaxy luminosity function. We find that ∼35% of the objects in the deep sample are Seyfert galaxies, rather than QSOs, having absolute magnitudes fainter than $M_B = -23$.

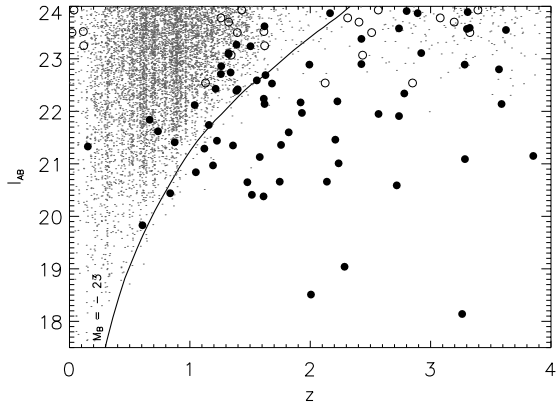

Fig. 8. Apparent I_{AB} magnitude as a function of redshift in the VVDS deep sample. Galaxies are plotted with points, BLAGN with secure redshift are plotted with filled dots and BLAGN with degenerate redshift are presented at all their redshift solutions with empty circles. The thick line gives the apparent magnitude of a BLAGN template of absolute magnitude $M_B = -23$ and therefore corresponds to the transition between the QSOs and Seyfert galaxies.

7. Morphology and color properties

The fundamental property of our survey is that it suffers neither from morphological nor from color-selection biases, which are present in most optical surveys. Therefore, using the VVDS deep photometric data, we are able, a posteriori, to quantitatively estimate the fraction of AGN missed by these standard selection criteria.

7.1. Morphological analysis

The use of a morphological selection of point-like objects causes the loss of BLAGN candidates for two main reasons. The first is due to the fact that a reliable separation between point-like and extended sources from ground-based data images is possible only for relatively bright objects. The second is linked to an intrinsic property of BLAGN: at relatively low z and low intrinsic luminosity, BLAGN may appear extended or at least slightly resolved because of significant contribution from the host galaxy. This effect can introduce a redshift-dependent bias in morphologically selected AGN samples, especially at faint magnitudes.

We conducted a morphological analysis of our BLAGN sample through the study of various shape parameters, which define a characteristic radius weighted by the light distribution function (Kron 1980). In particular, for this analysis we used the `SExtractor` flux-radius parameter, denoted as r_2, which approximately measures the radius that encloses half of the object's total light. This parameter is used to identify point-like sources, because, for unresolved objects, it is directly related to the width of the point spread function and it is independent of luminosity (for non-saturated objects). In the plane r_2, measured in I-band versus I-magnitude, we can distinguish two different classes of objects: unresolved sources that occupy a well-defined strip of the plane at small and approximately constant values of r_2 and resolved objects for which r_2 varies with magnitude.

This analysis is restricted to F02, F10, and F22 fields. We have excluded the CDFS for which this parameter is not measured. Since our data, covering large areas in different sky regions, were taken with different seeing conditions, the stellar locus resulting from the use of the measured r_2 values is significantly broadened, thus making a clear separation between point-like and extended objects difficult. To account for

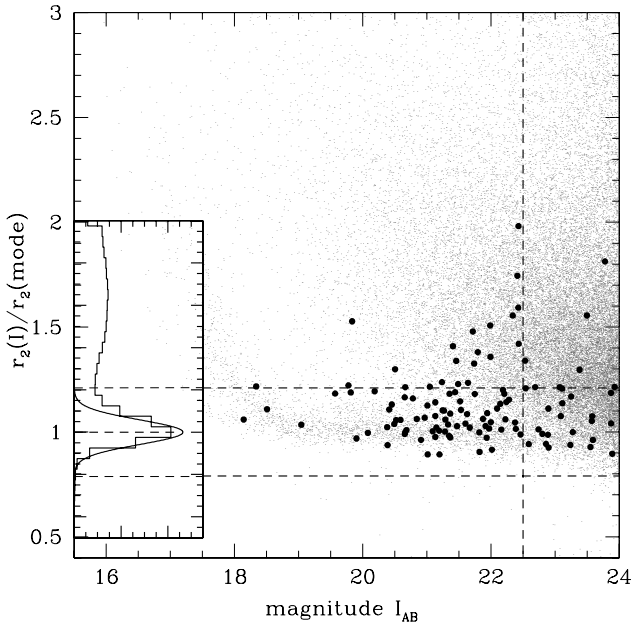

Fig. 9. Normalized $r_2(I)$ parameter versus I_{AB} magnitude. The two horizontal lines correspond to the range in $r_2(I)$ we adopted for our morphological classification of point-like sources. Large circles are the spectroscopically confirmed BLAGN. The inset shows the r_2 distribution of objects with $21.0 < I_{AB} < 22.0$, fitted with a Gaussian with $\sigma = 0.06$.

this, we used an "adaptive" classification technique following McCracken et al. (2003): after dividing the field into many subareas, mainly following the pattern corresponding to different pointings, we normalized the flux radius of each object to the local r_2 mode, computed for all the objects within each subarea. Figure 9 shows this normalized $r_2(I)$ parameter versus I-magnitude.

The use of the normalized $r_2(I)$ allows us to improve our ability to distinguish point-like from extended objects. As shown in Fig. 9, this separation appears feasible up to $I_{AB} \sim 22.5$ (without normalization the corresponding limiting magnitude was $I_{AB} \sim 21.5$). Beyond this magnitude ($I_{AB} \sim 22.5$), the number of galaxies with small $r_2(I)$ parameter increases and no reliable selection of point-like sources is possible.

The two horizontal lines correspond to the range in $r_2(I)$ that we adopted for our morphological classification of point-like sources. The upper limit in this range corresponds to about 3.5σ of the Gaussian fit of the r_2 normalized distribution of point-like sources. As shown by the inset in the left part of Fig. 9, this somewhat conservative choice makes certain that the vast majority of point-like sources are really classified as point-like, allowing some contamination from extended objects, especially at faint magnitude. Efficiency in classifying point-like sources was tested on the spectroscopically confirmed stars in the magnitude range $18.5 \leq I_{AB} \leq 22.5$; the bright limit was set in order to exclude saturated objects (see Fig. 9). We find that 95% of the stars with spectroscopic flag ≥ 3 (see Le Fèvre et al. 2005) are correctly classified as point-like sources.

Figure 9 also shows the location in this plane of the spectroscopically confirmed BLAGN. In this analysis we consider only BLAGN brighter than $I_{AB} = 22.5$ (90 objects); within this limit, 77% of the BLAGN are classified as point-like, while 21 of them (23%) are classified as extended. This percentage is significantly higher than that of morphologically misclassified stars (see above).

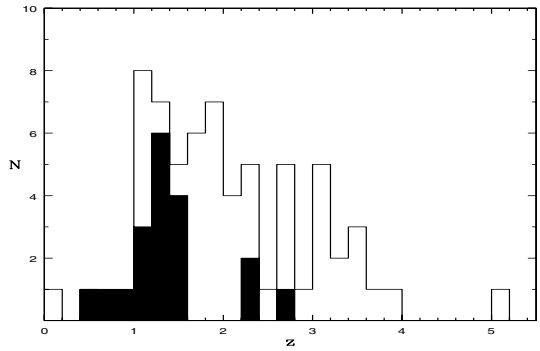

Fig. 10. Redshift distribution of BLAGN with secure redshift and $I_{AB} < 22.5$. The unshaded histogram shows the objects classified as point-like, while the filled histogram shows the objects classified as extended.

Nineteen of these 21 extended BLAGN have a secure redshift measurement, while the other 2 are BLAGN with two or more possible values for z. Figure 10 shows the redshift distribution of BLAGN with secure redshift and $I_{AB} \leq 22.5$, morphologically classified as extended compared to those classified as point-like. The two redshift distributions are significantly different (the probability that they are drawn from the same distribution, as estimated from a Kolmogorov-Smirnov (KS) test, is smaller than $\sim 4 \times 10^{-4}$), with the extended BLAGN having on average a lower redshift. The figure shows that sixteen out of nineteen of these BLAGN have $z < 1.6$, and in this redshift range they constitute ~42% of the sample.

7.2. Color analysis

The classical way to create an optical BLAGN sample is to preselect candidates from a photometric catalog requiring that the objects are point-like and have blue colors. This selection criterion allows us to select BLAGN candidates with an efficiency above 50% (see Croom et al. 2004), at least for objects brighter than $B \sim 21$. This jump in efficiency – from less than 1% in a flux-limited sample without preselection (see end of Sect. 3.1) to more than 50% with preselection – makes it possible to construct very large catalogs of several tens of thousands of BLAGN, such as the 2QZ.

The drawbacks of this selection criterion are:

(a) Its high redshift limit arises at about the same redshift than the observed cutoff of BLAGN space density, i.e. $z \sim 2.3$;
(b) It excludes objects at low redshift, for which the contribution of the host galaxy is detected and resolved, thus introducing a bias especially toward the faint end of the BLAGN luminosity function.

To overcome this problem, various surveys adopted more complex selection algorithms based on multicolor analysis, estimating for each of them different levels of incompleteness. The SDSS QSO survey is the largest example of this kind of survey. Its completeness function is investigated in detail in Vanden Berk et al. (2005).

We investigate here how a simple utraviolet excess preselection technique based on three color bands would have applied to our sample. For this purpose we used the deep photometry obtained in the frame of the CFHTLS and plotted our point-like objects in the color plane $u^* - g'$, $g' - r'$, as shown Fig. 11, left panel. We could then set a color selection criterion meant to exclude most of the main sequence stars: (a) $u^* - g' < 0.62$;

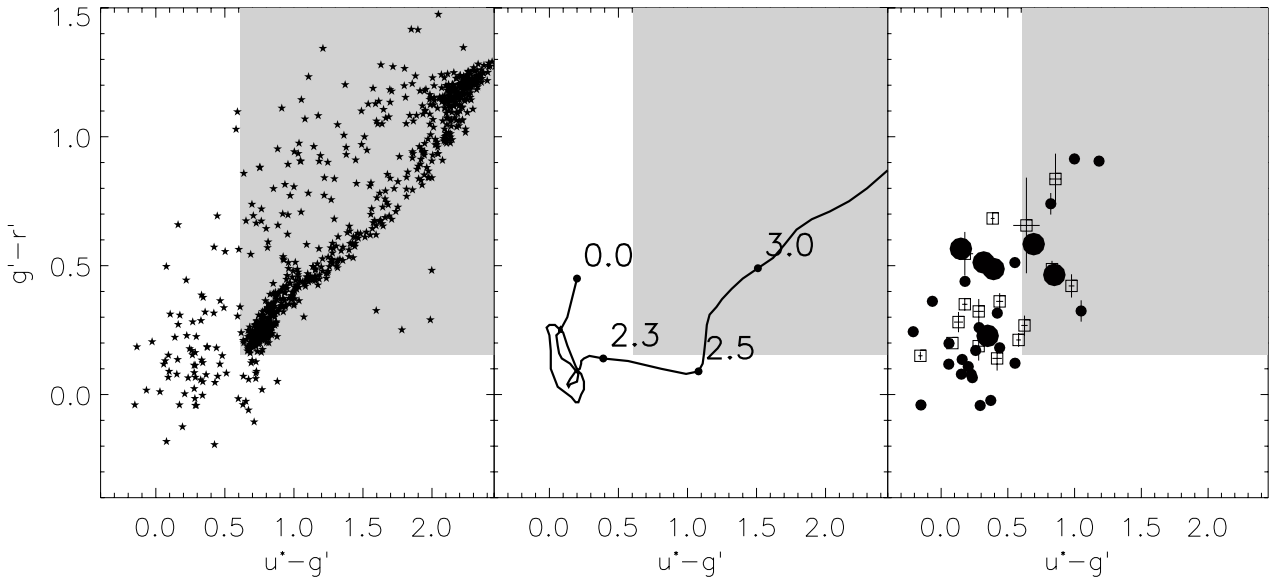

Fig. 11. The $u^* - g'$, $g' - r'$ color diagram. *Left panel*: location of the point-like objects in our photometric catalog. An exclusion area, reported in gray, is set to exclude most of the main sequence stars. *Middle panel*: color evolutionary track with redshift of a BLAGN. The template considered here is the SDSS composite spectrum. *Right panel*: location of AGN with $z < 2.3$. AGN that could not be morphologically classified ($I_{AB} > 22.5$) are plotted with open boxes. AGN classified as extended are big dots, while AGN classified as point-like are small dots.

(b) $g' - r' < 0.16$. The exclusion area is reported in Fig. 11. Most of the objects in the exclusion area, ouside the locus delineated by the main sequence stars, are compact galaxies classified as point-like objects.

Following the evolutionary track of a QSO template (here the SDSS composite spectrum, Vanden Berk et al. 2001) in this color plane, we can expect this selection criterion to be efficient up to $z \sim 2.3$–2.5.

We estimate now which fraction of the optical AGN population with $z < 2.3$ would have been missed by this selection criterion. Our AGN sample with $z < 2.3$ and photometric information in the u^*, g', and r' bands is reported in this plane (Fig. 11, right panel). We find that ∼25% of the population of our optical BLAGN would have been excluded by this color selection. If we now restrict our analysis to a limiting magnitude of $I_{AB} < 22.5$, we find that ∼35% of our AGN do not fulfill this color-selection criterion combined with a morphological selection of point-like objects. As expected, at higher redshift this selection criterion becomes inefficient, with 75% of our $z > 2.3$ objects excluded by this criterion. We would like to emphasize that these completeness rates are found for our sample that is two to three magnitude deeper than current major samples and do not necessarily apply to existing brighter samples.

Figure 12 presents the difference as a function of redshift between the $B_{AB} - I_{AB}$ colors of our BLAGN sample and the color expected for the SDSS composite spectrum for $z < 2.8$. The dispersion in color is large, and most of our objects have a significantly redder color than that expected from the SDSS composite spectrum. Moreover, the faintest objects appear to have redder colors on average than the brightest ones. A KS test applied on the color of the Seyfert galaxies ($M_B > -23$) and of the QSOs ($M_B < -23$) indicates a probability $\sim 1 \times 10^{-3}$ that these objects have the same color distribution.

This could be explained in different ways: (a) the contamination of the host galaxy is significantly reddening the measured colors of faint AGN; (b) BLAGN are intrinsically redder when they are faint; (c) the reddest color are due to the presence of dust. With the present analysis, we cannot exclude or confirm

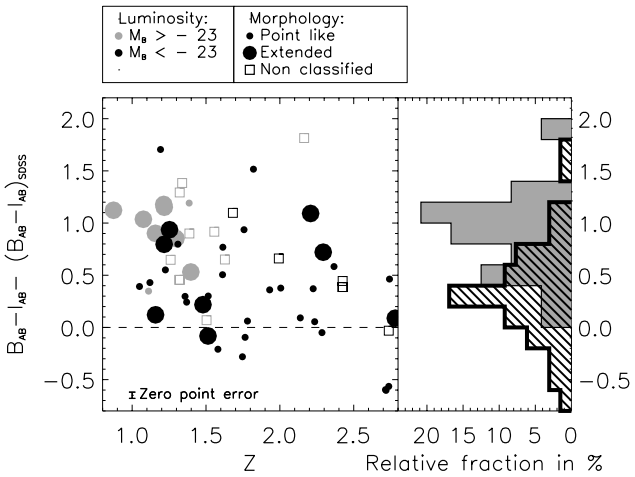

Fig. 12. Difference as a function of redshift between the observed $B_{AB} - I_{AB}$ colors and the color expected for the SDSS composite spectrum. Black dots correspond to QSOs, while the gray dots correspond to Seyfert galaxies. The $B_{AB} - I_{AB}$ color histograms of these two populations are shown on the right.

hypotheses (b) and (c). However, we observe that, for ∼50–60% of our reddest AGN (objects with $(B_{AB}-I_{AB})-(B_{AB}-I_{AB})_{SDSS} > 0.8$), we detect the extended component of the BLAGN host galaxy in I band. In this redshift range, the contribution from the host galaxies is in fact expected to be more significant in the I band (corresponding to near UV-B rest-frame bands) than in the B band (corresponding to the far UV rest-frame band). We therefore believe that host galaxy contamination is contributing to give a redder color to our BLAGN.

From this morphological and color analysis, we conclude that classical optical preselection techniques are significantly under-sampling the overall BLAGN population in deep samples. This effect should be fully taken into account when deriving BLAGN volume densities or related quantities.

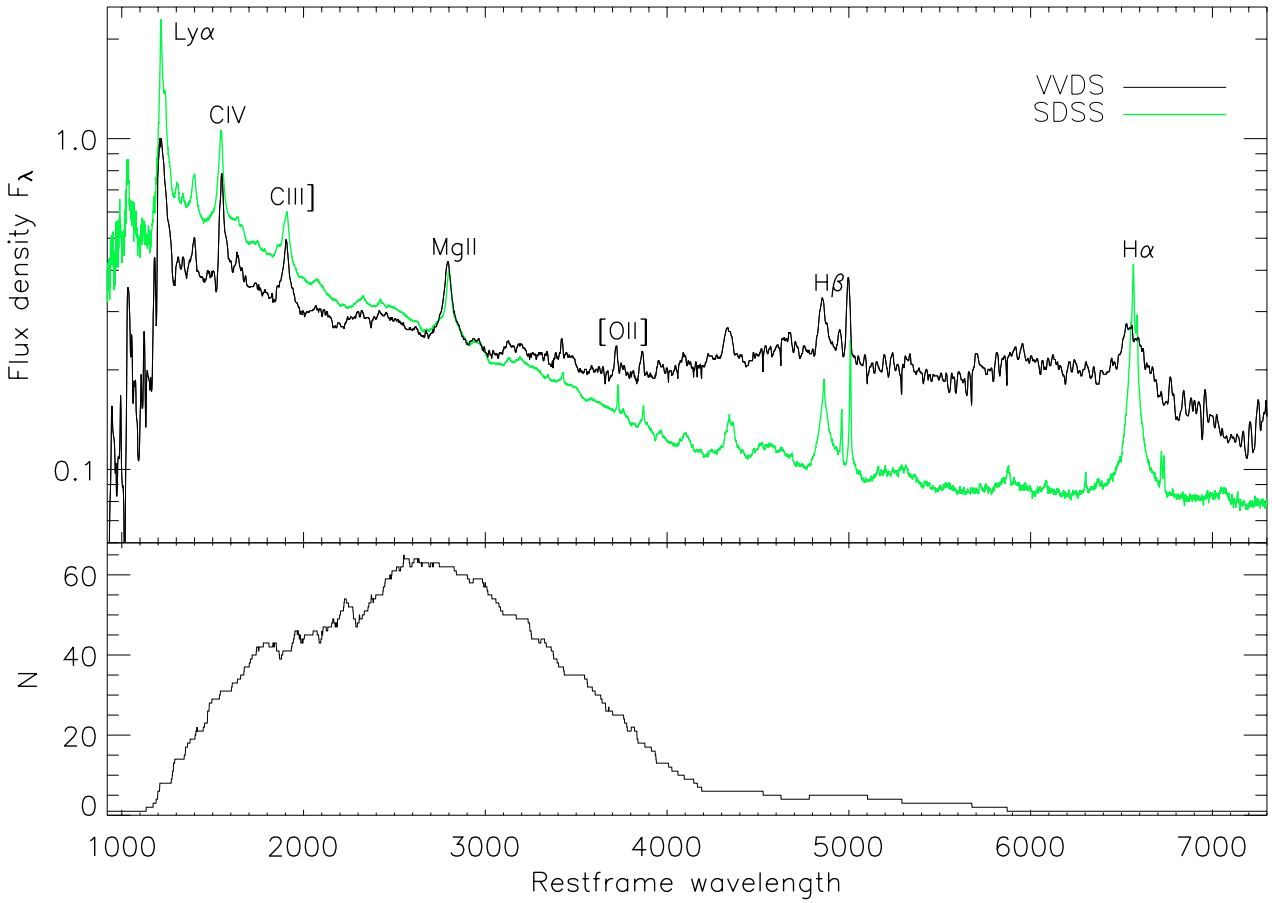

Fig. 13. Composite spectrum. *Top panel*: composite spectrum of the VVDS BLAGN with secure redshift (black) compared with the SDSS composite spectrum (gray or green in the electronic version). *Bottom panel*: number of contributing spectra as a function of wavelength.

8. Composite spectrum

A rest-frame composite spectrum was generated according to the method described in Francis et al. (1991). The spectra were first blue-shifted in their rest frame and rebinned to 1 Å. The lowest redshift spectrum was taken as a starting point for building the long wavelength part of the composite. The spectra were then taken in order of increasing redshift, and the spectral range in common with the composite was determined for each of them. The spectrum was rescaled to have the same average as the composite in this common spectral range. It was then added to the composite. Each contribution is weighted by the corresponding individual average *S/N*. The co-addition is a geometric mean to preserve the continuum logarithmic slope (see Francis et al. 1991). Once all spectra are co-added a sliding Gaussian filter (σ = 2 Å) is applied to the composite to improve the *S/N*.

Individual redshifts are slightly varied so as to maximize the peaks of each main emission line, then they are averaged and corrected to fix the line peaks close to their laboratory wavelengths. Then the entire procedure is iterated, the convergence being quite fast after 2 or 3 iterations. All 115 BLAGN spectra with secure redshifts but one have been used to generate the composite. In particular, BAL spectra are included. The spectrum of object 000029274 at redshift 0.7352, is strongly affected by the residual noise of the fringing pattern and contributes to a wavelength range covered by only 5 other objects. For this reason it was excluded to generate the composite. The final composite obtained is shown in Fig. 13 along with the number of contributing spectra. For comparison the SDSS composite spectrum obtained with the same method over 2200 spectra is plotted over our composite (Vanden Berk et al. 2001).

Table 3. Rest-frame equivalent widths and full-width half maximum of the VVDS composite spectrum compare to the SDSS composite spectrum.

line	λ_0	*EW*(VVDS)	*EW*(SDSS)
Ly_α + N V	1216 + 1240	137.4	92.91
Si IV + O IV]	1396 + 1402	7.9	8.13
C IV	1549	46.0	23.78
C III]	1909	25.5	21.19
Mg II	2798	40.3	32.28
[O II]	3727	3.4	1.56
[Ne III]	3869	2.7	1.38
H_δ	4103	5.0	5.05
H_γ	4342	21.8	12.62
H_β	4861	33.8	46.21
[O III]	4959	4.9	3.50
[O III]	5007	16.8	13.23
H_α	6562	137.5	194.52

The maximum number of individual spectra contributing to the composite is 64 near 2570 Å. At both wavelength ends, only a few objects contribute to the composite spectrum. The *S/N* is ~60 in the 2000–4000 Å range and goes down to ~30 at larger wavelength. We measured the EW of the main emission lines in the composite using the IRAF package[3]. Broad emission lines

[3] `http://iraf.noao.edu/`

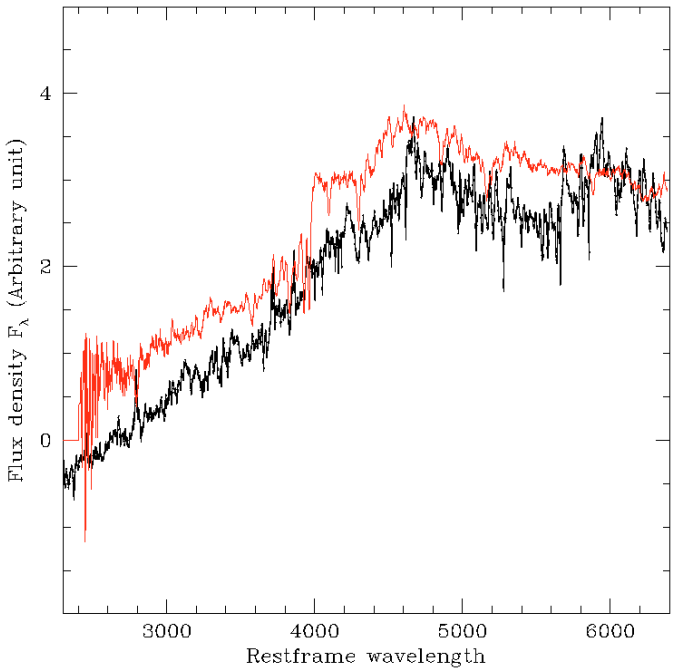

Fig. 14. Difference between VVDS-AGN composite spectrum and the SDSS one. For comparison, the red line shows the template of early type galaxies as derived from the VVDS data.

were fitted by a Lorentzian profile, while narrow emission lines were fitted by a Gaussian. C IV and Lyα lines were deblended from their absorption component. The resulting EW values are given Table 3 and are compared to those of the SDSS composite spectrum.

Significant differences are seen in the EW of Lyα and Hα. The reason for such discrepancies is likely to be the wide variety of EWs for the same line observed in QSO spectra, since very few objects contribute at both ends of the VVDS composite spectrum, 5 or less below 1200 Å and above 5050 Å. We interpret the larger EW we obtain for the C IV and the Mg II lines as a consequence of the Baldwin effect (Baldwin 1977), our objects being a factor up to 100 times fainter than the ones of the SDSS sample.

The overall continuum shape of our composite spectrum is redder than that of the SDSS composite, which is particularly true at $\lambda > 3000$ Å. This can again, indicate that the host galaxy contamination is reddening our composite spectrum at long wavelength. This result is consistent with the discussion in the section about the red colors we observe for our fainter objects. To further check this interpretation, a new composite was computed excluding the extended objects found in our morphological analysis above, for which we expect the contamination of the host galaxy to be stronger. This composite of point-like BLAGN was indeed found to have a bluer continuum than our composite with the complete sample.

Finally, we subtracted the continuum of the SDSS composite spectrum from that of the VVDS composite; emission lines have been previously fitted and subtracted from the composite spectrum. The resulting difference is shown in Fig. 14 together with the spectrum of the template of early type galaxies as derived from the VVDS data (Contini et al. 2006). The good agreement of the overall shape of the two spectra further strengthens our conclusion about the probable significant contamination of the red part of our composite spectrum by emission from the host galaxies.

9. Summary and conclusion

This paper describes a complete sample of 130 BLAGN selected from the VVDS first-epoch spectroscopic catalog down to $I_{AB} = 24$. It is the first spectroscopic BLAGN catalog of this size at such faint magnitudes that is purely magnitude limited and free of preselection biases.

The VVDS deep and wide complete samples contain 74 and 56 BLAGN, respectively, in this first release. A total of about 250 to 300 BLAGN are expected when the VVDS is completed. We measure cumulative surface densities of 472 ± 48 BLAGN per sq. deg. with $I_{AB} \leq 24$.

The redshift distribution ranges from 0 to 5, while the mean redshift in both the WIDE and DEEP samples is 1.8. By pushing our magnitude limit from $I_{AB} = 22.5$ to $I_{AB} = 24$, the result is not to increase the mean redshift of the sample, but rather to explore the faint end of the luminosity function at all redshifts.

By comparing the $u-g, g-r$ color distribution of our AGN population with $z < 2.3$ and $I_{AB} < 22.5$ to the complete VVDS photometric catalog of stellar-like objects, we find that ∼35% of the AGN present in our sample would be missed by the usual UV excess and morphological criteria used for the preselection of optical QSO candidates in this redshift range. Most of the extended VVDS BLAGN are below the redshift $z = 1.6$, a redshift range where 42% of VVDS BLAGN are extended.

The VVDS BLAGN have redder colors at the faint end of the luminosity function. Although we cannot exclude that the intrinsic spectrum of BLAGN is redder at faint luminosity or that the redder color is due to the presence of dust, there is evidence that this effect is due to contamination by the continuum of the host galaxy at faint magnitudes. Indeed, 35% of the VVDS BLAGN have magnitudes fainter than $M_B = -23$.

This contamination is also seen in the composite spectrum obtained by co-adding the individual spectra in their rest frame. A comparison of the VVDS and SDSS composite QSO spectra shows that the VVDS continuum is significantly redder than the SDSS one, especially at long wavelengths.

In the context of the study of the VVDS luminosity function and its evolution (Bongiorno et al. 2006), our BLAGN sample has two interesting properties. First, it is free of biases in the redshift range $2 < z < 3$, which will help to shed light on the change of QSO evolution suspected to happen in this redshift range. Second, since no bias against low-luminosity AGN is present in this sample, it will be easier to compare of the evolution of low and high luminosity AGN, allowing a better understanding of the QSO-Seyfert connection.

Acknowledgements. This research was developed within the framework of the VVDS consortium. This work was partially supported by the CNRS-INSU and its Programme National de Cosmologie (France), and by Italian Ministry (MIUR) grants COFIN2000 (MM02037133) and COFIN2003 (2003020150). The VLT-VIMOS observations were been carried out on guaranteed time (GTO) allocated by the European Southern Observatory (ESO) to the VIRMOS consortium, under a contractual agreement between the Centre National de la Recherche Scientifique of France, heading a consortium of French and Italian institutes, and ESO, to design, manufacture, and test the VIMOS instrument. It is based on observations obtained with MegaPrime/MegaCam, a joint project of the CFHT and CEA/DAPNIA, at the Canada-France-Hawaii Telescope (CFHT), which is operated by the National Research Council (NRC) of Canada, the Institut National des Sciences de l'Univers of the Centre National de la Recherche Scientifique (CNRS) of France, and the University of Hawaii. This work is based in part on data products produced at TERAPIX and the Canadian Astronomy Data Center as part of the Canada-France-Hawaii Telescope Legacy Survey, a collaborative project of the National Research Council (NRC) of Canada and of the Centre National de la Recherche Scientifique (CNRS) of France.

References

Arnouts, S., Vandame, B., Benoist, C., et al. 2001, A&A, 379, 740
Arnouts, S., Schiminovich, D., Ilbert, O., et al. 2005, ApJ, 619, L43
Avni, Y., & Bahcall, J. N. 1980, ApJ, 235, 694A
Baldwin, J. A. 1977, ApJ, 214, 679
Bondi, M., Ciliegi, P., Zamorani, G., et al. 2003, A&A, 403, 857
Bongiorno, et al. 2006, in preparation
Bottini, D., Garilli, B., Maccagni, D., et al. 2005, PASP, 117, 996
Brunzendorf, J., & Meusinger, H. 2002, A&A, 390, 879
Contini, et al. 2006, in preparation
Croom, S. M., Smith, R. J., Boyle, B. J., et al. 2004, MNRAS, 349, 1397
Francis, P. J., Hewett, P. C., Foltz, C. B., et al. 1991, ApJ, 373, 465
Garilli, et al. 2006, in preparation
Gehrels, N. 1986, ApJ, 303, 336
Hasinger, G., Miyaji, T., & Schmidt, M. 2005, A&A, 441, 417
Hewett, P. C., Foltz, C. B., & Chaffee, F. H. 1995, AJ, 109, 1498
Ilbert, O., Tresse, L., Zucca, E., et al. 2005, A&A, 439, 863
Iovino, A., McCracken, H. J., Garilli, B., et al. 2005, A&A, 442, 423
Ivezić, Ž., Menou, K., Knapp, G. R., et al. 2002, AJ, 124, 2364
Jackson, C. A., Wall, J. V., Shaver, P. A., et al. 2002, A&A, 386, 97
Jiang, L., Fan, X., Cool, R. J., et al. 2006, AJ, 131, 2788
Kron, R. G. 1980, ApJS, 43, 305
Le Fèvre, O., Saisse, M., Mancini, D., et al. 2003, SPIE, 4841, 1670
Le Fèvre, O., Mellier, Y., McCracken, H. J., et al. 2004, A&A, 417, 839
Le Fèvre, O., Vettolani, G., Garilli, B., et al. 2005, A&A, 439, 845
McCracken, H. J., Radovich, M., Bertin, E., et al. 2003, A&A, 410, 17
Miyaji, T., Hasinger, G., & Schmidt, M. 2000, A&A, 353, 25
Pierre, M., Valtchanov, I., Altieri, B., et al. 2004, J. Cosmol. Astro-Part. Phys., 9, 11
Pollo, A., Meneux, B., Guzzo, L., et al. 2005, A&A, 439, 887
Radovich, M., Arnaboldi, M., Ripepi, V., et al. 2004, A&A, 417, 51
Richards, G. T., Fan, X., Newberg, H. J., et al. 2002, AJ, 123, 2945
Sandage, A., & Wyndham, J. D. 1965, ApJ, 141, 328
Schade, D., Crampton, D., Hammer, F., Le Fèvre, O., & Lilly, S. J. 1996, MNRAS, 278, 95
Schiminovich, D., Ilbert, O., Arnouts, S., et al. 2005, ApJ, 619, L47
Schlegel, D. J., Finkbeiner, D. P., & Davis, M. 1998, ApJ, 500, 525
Scodeggio, M., Franzetti, P., Garilli, B., et al. 2005, A&A, 000, 00
Szokoly, G. P., Bergeron, J., Hasinger, G., et al. 2004, ApJS, 155, 271
Ueda, Y., Akiyama, M., Ohta, K., & Miyaji, T. 2003, ApJ, 598, 886
Vanden Berk, D. E., Richards, G. T., Bauer, A., et al. 2001, AJ, 122, 549
Vanden Berk, D. E., Schneider, D. P., Richards, G. T., et al. 2005, AJ, 129, 2047
Wall, J. V., Jackson, C. A., Shaver, P. A., Hook, I. M., & Kellermann, K. I. 2005, A&A, 434, 133
Wisotzki, L., Christlieb, N., Bade, N., et al. 2000, A&A, 358, 77
Wolf, C., Wisotzki, L., Borch, A., et al. 2003, A&A, 408, 499

Online Material

Appendix A: Catalog tables

Table A.1. BLAGN with secure redshift (flags 14 and 13).

Object ID	α_{J2000}	δ_{J2000}	z	flag	I_{AB}	B_{AB}	V_{AB}	R_{AB}	Morphology$^{(*)}$
CDFS:	deep mode	10 AGN							
000037103	$03^h32^m37.47^s$	$-27°40^m00.33^s$	0.6656	14	21.84	–	–	–	–
000037399	$03^h32^m38.14^s$	$-27°39^m45.02^s$	0.8366	14	20.44	–	–	–	–
000073509	$03^h32^m02.47^s$	$-27°46^m00.53^s$	1.6199	$14^{(S)}$	23.62	–	–	–	–
000023526	$03^h32^m43.25^s$	$-27°49^m14.38^s$	1.9199	$14^{(S)}$	22.17	–	–	–	–
000028880	$03^h33^m03.62^s$	$-27°45^m18.97^s$	1.2574	14	22.71	–	–	–	–
000029274	$03^h32^m30.23^s$	$-27°45^m04.75^s$	0.7352	14	21.62	–	–	–	–
000018607	$03^h32^m18.26^s$	$-27°52^m41.42^s$	2.8010	14	23.91	–	–	–	–
000025363	$03^h32^m59.85^s$	$-27°47^m48.42^s$	2.5673	14	21.95	–	–	–	–
000033629	$03^h32^m25.17^s$	$-27°42^m19.05^s$	1.6207	14	22.14	–	–	–	–
000031947	$03^h32^m00.37^s$	$-27°43^m19.85^s$	1.0401	$14^{(S)}$	22.12	–	–	–	–
0226-04	deep mode	56 AGN							
020176565	$02^h25^m28.06^s$	$-04°36^m41.59^s$	1.5039	14	23.24	23.62	23.61	23.26	–
020158952	$02^h26^m17.81^s$	$-04°39^m08.50^s$	0.8738	14	21.41	22.82	22.16	21.99	extended
020086859	$02^h26^m29.62^s$	$-04°49^m14.41^s$	1.1921	13	20.97	22.98	21.97	21.43	point-like
020213000	$02^h26^m47.88^s$	$-04°31^m35.20^s$	1.2250	13	21.44	22.30	22.02	21.76	point-like
020212038	$02^h26^m08.40^s$	$-04°31^m43.15^s$	2.2082	$14^{(F)}$	21.46	22.91	22.27	22.02	extended
020131908	$02^h26^m51.04^s$	$-04°42^m56.55^s$	2.7813	14	22.34	23.08	22.75	22.76	extended
020210524	$02^h27^m07.55^s$	$-04°32^m02.98^s$	1.5150	14	20.41	21.03	20.90	20.64	point-like
020120394	$02^h26^m59.92^s$	$-04°44^m30.32^s$	1.6120	14	20.38	21.27	20.96	20.78	point-like
020114448	$02^h27^m00.99^s$	$-04°45^m16.83^s$	1.6140	13	22.24	23.39	23.35	22.97	point-like
020118986	$02^h26^m54.53^s$	$-04°44^m37.72^s$	3.3018	14	23.57	25.42	23.98	23.97	–
020118483	$02^h27^m36.06^s$	$-04°44^m41.89^s$	1.2606	13	22.86	23.82	23.44	23.30	–
020188089	$02^h25^m25.68^s$	$-04°35^m09.45^s$	2.1384	14	20.66	21.12	20.94	20.95	point-like
020147295	$02^h25^m29.19^s$	$-04°40^m44.16^s$	1.5562	$14^{(F)}$	22.59	23.87	23.44	22.84	–
020169816	$02^h25^m45.04^s$	$-04°37^m35.95^s$	3.5893	$14^{(F)}$	22.14	24.67	22.95	22.64	point-like
020190479	$02^h25^m45.55^s$	$-04°34^m45.18^s$	0.1524	14	21.33	21.99	21.55	21.64	point-like
020268754	$02^h26^m09.63^s$	$-04°24^m37.74^s$	2.7187	14	20.59	20.56	20.60	20.75	point-like
020164607	$02^h25^m32.46^s$	$-04°38^m18.63^s$	2.9220	14	23.11	23.92	23.46	23.21	–
020179116	$02^h25^m34.98^s$	$-04°36^m16.46^s$	3.3080	$14^{(F)}$	23.89	25.18	23.94	23.84	–
020237445	$02^h25^m57.38^s$	$-04°28^m46.04^s$	1.2138	14	22.43	23.92	23.53	23.06	extended
020223153	$02^h26^m17.52^s$	$-04°30^m29.27^s$	1.4777	$14^{(F)}$	20.65	21.18	21.05	20.94	point-like
020163018	$02^h26^m45.20^s$	$-04°38^m30.58^s$	1.3208	$14^{(F)}$	23.11	23.89	23.62	23.29	–
020180665	$02^h26^m45.46^s$	$-04°36^m15.43^s$	3.2619	14	18.14	21.09	19.32	19.03	point-like
020177875	$02^h26^m53.87^s$	$-04°36^m27.21^s$	1.6821	13	22.53	24.01	23.65	23.36	–
020234610	$02^h26^m58.99^s$	$-04°29^m06.02^s$	2.1645	13	23.87	26.05	25.11	24.74	–
020159510	$02^h27^m09.85^s$	$-04°39^m02.21^s$	1.9309	14	21.97	22.73	22.41	22.44	point-like
020218399	$02^h27^m31.34^s$	$-04°30^m50.26^s$	2.2255	14	22.19	22.91	22.39	22.53	point-like
020254511	$02^h27^m36.93^s$	$-04°26^m31.30^s$	1.7466	14	20.66	20.76	20.84	20.85	point-like
020243922	$02^h27^m47.33^s$	$-04°27^m53.20^s$	1.1203	14	21.29	22.02	21.71	21.60	point-like
020165108	$02^h26^m59.85^s$	$-04°38^m12.68^s$	1.3219	13	23.09	24.70	24.04	23.78	–
020179225	$02^h27^m02.15^s$	$-04°36^m15.96^s$	1.3860	13	22.39	23.90	23.50	23.01	point-like
020195823	$02^h27^m24.10^s$	$-04°33^m55.72^s$	2.4250	$14^{(F)}$	23.38	24.19	23.61	23.85	–
020254576	$02^h25^m27.23^s$	$-04°26^m31.02^s$	3.8527	14	21.15	23.33	21.78	21.44	point-like
020200020	$02^h25^m50.40^s$	$-04°33^m24.00^s$	2.7373	13	21.91	21.95	22.10	21.73	point-like
020329650	$02^h26^m08.71^s$	$-04°16^m34.53^s$	1.0498	14	20.84	21.52	21.14	20.96	point-like
020232397	$02^h26^m26.04^s$	$-04°29^m27.88^s$	1.6280	$14^{(F)}$	22.69	23.72	23.31	23.15	–
020461765	$02^h26^m35.95^s$	$-04°23^m21.81^s$	3.2831	14	22.89	24.62	23.01	22.87	–
020466135	$02^h26^m46.99^s$	$-04°18^m37.56^s$	1.5806	14	21.13	21.29	21.56	21.05	point-like
020467962	$02^h26^m59.17^s$	$-04°16^m55.89^s$	3.3247	13	23.59	25.22	23.96	23.80	–
020461459	$02^h27^m04.25^s$	$-04°23^m37.77^s$	1.8211	13	21.60	23.50	22.92	22.41	point-like
020465339	$02^h27^m06.44^s$	$-04°19^m24.30^s$	3.2852	14	21.09	21.77	21.31	20.99	point-like
020467628	$02^h27^m04.06^s$	$-04°17^m09.77^s$	1.3582	13	21.35	21.97	21.82	21.61	point-like
020205812	$02^h27^m23.84^s$	$-04°32^m31.69^s$	2.8922	14	23.87	24.77	24.36	24.52	–
020208084	$02^h27^m29.24^s$	$-04°32^m27.51^s$	2.2850	$14^{(F)}$	19.04	19.34	19.10	19.12	point-like
020277536	$02^h27^m53.85^s$	$-04°23^m20.10^s$	3.6260	14	23.55	25.25	23.88	23.60	–
020278210	$02^h27^m40.00^s$	$-04°23^m17.43^s$	1.7574	13	21.36	22.68	21.87	22.28	point-like
020239945	$02^h27^m31.14^s$	$-04°28^m22.83^s$	2.4247	$14^{(F)}$	22.90	23.65	23.13	23.14	–
020351846	$02^h26^m30.84^s$	$-04°13^m26.09^s$	3.5680	$14^{(F)}$	22.80	25.05	23.71	23.24	–
020367106	$02^h26^m34.71^s$	$-04°11^m33.98^s$	1.3973	$14^{(F)}$	22.42	23.28	23.02	22.55	extended
020351277	$02^h25^m57.41^s$	$-04°13^m39.43^s$	0.6061	14	19.83	20.60	20.39	20.32	extended
020258622	$02^h26^m20.06^s$	$-04°25^m54.51^s$	1.3386	14	22.74	24.45	23.84	23.46	–

Table A.1. continued.

Object ID	α_{J2000}	δ_{J2000}	z	flag	I_{AB}	B_{AB}	V_{AB}	R_{AB}	Morphology$^{(*)}$
020286836	$02^h26^m22.17^s$	$-04°22^m21.62^s$	2.0060	14	18.51	19.28	19.11	19.05	point-like
020291309	$02^h26^m31.23^s$	$-04°21^m28.87^s$	1.9930	14	22.89	23.95	23.56	23.81	–
020465540	$02^h26^m44.48^s$	$-04°19^m16.76^s$	2.7372	14	23.58	24.15	23.94	23.81	–
020302785	$02^h26^m24.63^s$	$-04°20^m02.14^s$	2.2357	14	21.01	21.42	21.26	21.34	point-like
020364478	$02^h26^m49.41^s$	$-04°11^m53.30^s$	1.1573	14	21.74	22.94	22.74	22.25	extended
020463196	$02^h27^m00.65^s$	$-04°21^m49.00^s$	1.3875	14	23.27	24.49	24.42	23.91	–
1003+01	wide mode	18 AGN							
100122852	$10^h02^m11.17^s$	$+01°22^m28.58^s$	1.8007	14	19.86	–	–	–	point-like
100110223	$10^h02^m48.14^s$	$+01°20^m02.29^s$	1.8255	13	21.30	–	–	–	point-like
100210521	$10^h03^m27.33^s$	$+01°35^m50.91^s$	1.1723	14	21.59	22.05	21.73	21.56	point-like
100139500	$10^h02^m57.37^s$	$+01°25^m40.38^s$	1.2478	13	20.96	–	–	–	point-like
100126868	$10^h03^m08.80^s$	$+01°23^m16.56^s$	2.3302	14	20.34	–	–	–	point-like
100105943	$10^h03^m46.33^s$	$+01°19^m11.04^s$	3.5553	13	21.15	–	–	–	point-like
100290682	$10^h03^m11.33^s$	$+01°47^m01.56^s$	1.5487	$14^{(F)}$	21.45	–	–	–	extended
100327652	$10^h03^m13.81^s$	$+01°52^m13.97^s$	1.2173	14	22.39	23.85	23.43	22.90	extended
100232259	$10^h03^m30.37^s$	$+01°38^m51.18^s$	1.7647	14	21.09	21.37	21.30	21.33	point-like
100190464	$10^h04^m25.14^s$	$+01°33^m07.74^s$	1.0760	14	21.66	22.98	22.38	22.41	extended
100168207	$10^h04^m36.55^s$	$+01°30^m05.86^s$	2.7152	14	22.40	22.38	21.84	22.14	point-like
100113463	$10^h04^m07.25^s$	$+01°20^m38.90^s$	1.8436	14	20.47	–	–	–	point-like
100123590	$10^h04^m46.72^s$	$+01°22^m39.10^s$	2.0963	13	21.47	–	–	–	point-like
100343840	$10^h04^m32.08^s$	$+01°54^m24.12^s$	2.3666	$14^{(F)}$	19.75	20.68	20.40	20.15	point-like
100338914	$10^h04^m13.45^s$	$+01°53^m41.38^s$	1.1584	14	19.73	20.15	19.80	19.78	extended
100245809	$10^h04^m00.36^s$	$+01°40^m45.74^s$	3.0789	14	21.62	22.71	22.01	21.94	point-like
100241696	$10^h04^m11.84^s$	$+01°40^m06.47^s$	1.1112	13	21.95	22.59	21.89	22.19	point-like
100451895	$10^h04^m38.01^s$	$+02°09^m25.07^s$	1.7806	13	20.03	20.46	20.31	20.36	point-like
2217+00	wide mode	31 AGN							
220586430	$22^h14^m34.82^s$	$+00°19^m24.18^s$	1.0285	14	20.35	–	–	–	point-like
220568559	$22^h14^m43.23^s$	$+00°14^m16.29^s$	1.4980	13	22.10	–	–	–	point-like
220566905	$22^h14^m02.39^s$	$+00°13^m49.58^s$	1.5285	13	22.28	–	–	–	point-like
220554336	$22^h14^m44.17^s$	$+00°10^m02.54^s$	0.4470	14	21.02	–	–	–	point-like
220001963	$22^h13^m51.58^s$	$+00°25^m01.30^s$	2.6801	14	22.19	–	–	–	point-like
220010371	$22^h14^m28.40^s$	$+00°27^m32.40^s$	3.6952	14	21.79	–	–	–	point-like
220056847	$22^h14^m48.77^s$	$+00°41^m16.67^s$	3.0015	14	21.38	–	–	–	point-like
220567825	$22^h15^m08.48^s$	$+00°14^m04.38^s$	1.1601	13	21.07	–	–	–	point-like
220576817	$22^h15^m09.17^s$	$+00°16^m42.38^s$	3.0957	14	21.81	–	–	–	point-like
220536609	$22^h15^m31.65^s$	$+00°04^m18.31^s$	0.4970	14	21.10	–	–	–	extended
220041929	$22^h15^m09.54^s$	$+00°36^m39.11^s$	1.4751	13	18.24	–	–	–	extended
220090821	$22^h15^m46.25^s$	$+00°50^m58.51^s$	1.8326	13	20.40	–	–	–	point-like
220082140	$22^h15^m32.40^s$	$+00°48^m36.29^s$	1.8484	$14^{(F)}$	20.58	–	–	–	point-like
220055529	$22^h15^m54.10^s$	$+00°40^m55.47^s$	3.5941	13	21.42	–	–	–	point-like
220567863	$22^h16^m27.06^s$	$+00°14^m02.32^s$	2.1610	14	20.80	–	–	–	point-like
220567224	$22^h16^m44.02^s$	$+00°13^m48.54^s$	5.0042	14	20.07	–	22.90	–	point-like
220591287	$22^h16^m49.05^s$	$+00°20^m46.27^s$	1.2968	$14^{(F)}$	22.30	23.47	23.32	–	extended
220580912	$22^h15^m56.66^s$	$+00°17^m52.28^s$	3.0432	13	22.11	–	–	–	point-like
220107230	$22^h16^m56.10^s$	$+00°56^m00.77^s$	1.0937	13	21.64	–	–	–	point-like
220575888	$22^h17^m36.55^s$	$+00°16^m23.09^s$	3.0755	14	21.25	22.16	21.50	–	point-like
220556037	$22^h17^m05.53^s$	$+00°10^m19.85^s$	2.7422	14	19.46	20.52	20.29	–	point-like
220542377	$22^h17^m10.42^s$	$+00°06^m04.72^s$	1.3097	13	21.12	22.24	21.95	–	point-like
220554600	$22^h17^m36.64^s$	$+00°10^m05.86^s$	1.3689	$14^{(F)}$	20.65	21.21	21.00	–	point-like
220544855	$22^h17^m39.71^s$	$+00°06^m52.80^s$	2.2934	$14^{(F)}$	20.91	21.97	21.61	–	extended
220044408	$22^h17^m34.47^s$	$+00°37^m33.52^s$	2.9096	$14^{(F)}$	21.18	21.65	21.54	–	point-like
220093875	$22^h17^m48.64^s$	$+00°51^m50.39^s$	1.3365	$14^{(F)}$	21.83	–	–	–	point-like
220081925	$22^h18^m00.42^s$	$+00°48^m31.41^s$	1.2167	13	21.68	22.79	22.40	–	extended
220609820	$22^h18^m29.04^s$	$+00°20^m24.32^s$	1.4794	$14^{(F)}$	21.52	22.04	21.86	–	extended
220610034	$22^h18^m14.20^s$	$+00°20^m49.73^s$	1.5135	$14^{(F)}$	20.54	20.77	20.86	–	extended
220613346	$22^h18^m33.73^s$	$+00°27^m09.76^s$	1.2530	$14^{(F)}$	20.39	21.63	21.25	–	extended
220098629	$22^h18^m01.51^s$	$+00°53^m19.83^s$	2.5790	$14^{(F)}$	21.71	–	–	–	point-like

$^{(*)}$ Morphological classification for objects with $I_{AB} < 22.5$. Objects in the VVDS-CDFS field are not classified. See Sect. 7.1.
$^{(F)}$ AGN re-observed in the 3800−6500 range with FORS1 in our follow-up program.
$^{(S)}$ Redshift confirmed by matching the catalog from Szokoly et al. (2004).

Table A.2. AGN with a single emission line detected (flag 19).

Object ID	α_{J2000}	δ_{J2000}	λ_{BL}	z solutions	I_{AB}	B_{AB}	V_{AB}	R_{AB}	Morphology(*)
CDFS:	deep mode	2 AGN							
000031270	$03^h32^m57.74^s$	$-27°43^m50.12^s$	7319.	0.1150[a] 1.6150[b]	23.52	–	–	–	–
000017025	$03^h31^m54.30^s$	$-27°53^m49.58^s$	6500.	1.3220[b] 2.4050[c] 3.1960[d]	23.70	–	–	–	–
0226-04:	deep mode	6 AGN							
020137737	$02^h26^m47.76^s$	$-04°42^m04.06^s$	6320.	1.2580[b] 2.3110[c] 3.0800[d]	23.78	24.58	24.14	24.16	–
020225567	$02^h27^m06.42^s$	$-04°30^m14.34^s$	6558.	1.3430[b] 2.4350[c]	23.07	24.65	24.26	23.74	–
020281035	$02^h26^m12.30^s$	$-04°22^m51.63^s$	6805.	0.0370[a] 1.4310[b] 2.5650[c] 3.3930[d]	23.93	25.06	24.39	24.07	–
020375508	$02^h25^m48.99^s$	$-04°10^m28.04^s$	5963.	1.1300[b] 2.1240[c] 2.8500[d]	22.54	23.25	22.98	23.04	–
020293248	$02^h26^m25.92^s$	$-04°21^m12.73^s$	7335.	0.1180[a] 1.6210[b]	23.25	24.79	24.54	24.13	–
020469530	$02^h26^m49.92^s$	$-04°15^m17.44^s$	6701.	0.0210[a] 1.3940[b] 2.5100[c] 3.3260[d]	23.50	24.69	24.35	24.28	–
2217+00:	wide mode	7 AGN							
220593613	$22^h14^m11.61^s$	$+00°21^m29.15^s$	6893.	0.0500[a] 1.4630[b] 2.6110[c]	21.90	–	–	–	extended
220056092	$22^h13^m53.81^s$	$+00°41^m06.90^s$	6100.	1.1790[b] 2.1950[c]	22.08	–	–	–	point-like
220583713	$22^h15^m34.70^s$	$+00°18^m42.01^s$	7352.	0.1200[a] 1.6270[b]	21.88	–	–	–	point-like
220548678	$22^h15^m02.71^s$	$+00°08^m10.56^s$	6766.	0.0310[a] 1.4170[b] 2.5440[c]	21.97	–	–	–	point-like
220023681	$22^h17^m46.44^s$	$+00°31^m26.58^s$	6956.	0.0600[a] 1.4850[b] 2.6440[c]	21.71	24.33	23.25	–	point-like
220551735	$22^h18^m05.78^s$	$+00°09^m12.66^s$	8056.	0.2270[a] 1.8780[b]	21.12	21.73	21.72	–	point-like
220234909	$22^h18^m13.40^s$	$+00°48^m54.05^s$	6407.	1.2890[b] 2.3560[c] 3.1360[d]	21.88	23.40	22.55	–	extended

(*) Morphological classification for objects with $I_{AB} < 22.5$. Objects in the VVDS-CDFS field are not classified. See Sect. 7.1.

[a] Emission line identified as Hα.

[b] Emission line identified as MgII.

[c] Emission line identified as C III].

[d] Emission line identified as CIV.